Linearization Point and Frequency Selection for Complex-Valued Electrical Capacitance Tomography

OPEN ACCESS

Linearization Point and Excitation Frequency Selection for Complex-Valued ECT

Liying Zhu, Lu Ma, Yi Li, Yunjie Yang, *Member, IEEE* and Maomao Zhang, *Member, IEEE*

Abstract—**Benefiting from the ability to image the permittivity distribution of dielectric materials, electrical capacitance tomography (ECT) has been applied for multiphase flow metering for decades as a contactless method. However, the water-continuous flow brings challenges for ECT since the conductivity in water makes ECT fail to reconstruct the distribution. Therefore, complex-valued ECT (CV-ECT) is introduced to image both permittivity and conductivity distribution based on complex-valued capacitance measurements using the same sensor head of ECT. Different from conventional ECT, the investigation of excitation frequency and linearization point selection is vital for CV-ECT, as the conductivity information is coupled with permittivity and frequency. An 8-electrode CV-ECT system was set up to obtain measurements both in simulations and experiments. The measurements on different phantoms over different excitation frequencies were conducted and the images were reconstructed to elaborate the selection of the linearization point and excitation frequency range.**

Index Terms—**Complex-valued measurement, Electrical capacitance tomography, Image reconstruction, Multi-frequency tomography**

I. INTRODUCTION

Electrical capacitance tomography (ECT) is known as a noninvasive imaging technique used to reconstruct the permittivity distribution of dielectric materials [1]. In conventional ECT, the capacitance measurements ignore the conductivity information and are mainly dependent on the permittivity within the region of interest (ROI). So, it is challenging for conventional ECT to measure the conductive phase of conductive/dielectric mixed multi-phase flows when the measurements are mainly dependent on the conductivity of water rather than the permittivity [2]. To address this issue, some multi-modality tomography systems such as ECT/electrical resistance tomography (ERT) dual-modality and ECT/magnetic induction tomography (MIT) dual-modality systems have been proposed [3-5], where ERT and MIT are used to provide conductivity information. Electrical impedance tomography (EIT) is another imaging technique widely used in medical imaging that can obtain complex impedance information [6]. In [7-9], a capacitively coupled ERT (CCERT)

is proposed and applied to image the conductivity distribution without contact with liquids, which can be regarded as the combination of ECT and ERT because it applied ECT sensors to collect resistance information. In [10, 11], phase information of complex admittance is used to reconstruct electrical parameter distribution, such as loss factor or permittivity. In [2, 12], a complex-valued, multi-frequency ECT (CVMF-ECT) system is proposed for simultaneous reconstruction of permittivity and conductivity using complex admittance data. Overall, these systems aim to utilize the complex admittance information rather than just capacitance information or resistance information via contactless methods.

As a time-difference imaging method [13], CV-ECT utilize the capacitance difference between the measurement under current flow phantom and the measurement under full pipe with background material. For air-water two phase flows, both air and water can be regarded as the background, *i.e.*, the linearization point of sensitivity. The final reconstruction results to a great extent depend on which linearization point is selected. Besides, different from the conventional ECT, the measurements of CV-ECT are frequency-dependent when conductive water is in the ROI. To obtain better reconstruction results, the excitation frequency should also be carefully selected.

In this paper, firstly the feasibility of CV-ECT system is verified by both simulation and experimental results. Secondly a method is proposed to estimate the optimal excitation frequency according to the water conductivity, this is vital in guiding the measuring circuits design of CV-ECT systems for different applications. Finally, the choice of the linearization point as well as the appropriate range of excitation frequency are discussed.

The CV-ECT model are briefly reviewed in Section II. And in Section III and IV, simulations and experiments were carried to investigate the appropriate selection of the linearization point and excitation frequency. Conclusions and future work are given in Section V.

II. FORWARD MODEL AND INVERSE SOLVER

The conventional ECT utilizes capacitance measurements to reconstruct the distribution of permittivity. The relationship

between the capacitance and permittivity can be demonstrated as:

$$C = -\frac{1}{V} \iint_S \varepsilon(x,y)\nabla\phi(x,y)\, d\Gamma \qquad (1)$$

where C and V denote the capacitance and potential difference between pairs of electrodes. $\varepsilon(x,y)$ and $\phi(x,y)$ is the permittivity and electrical potential distribution. And the surface integral is performed over the corresponding electrode area S. By introducing a perturbation of permittivity, the linear approximation form of Eq.(1) can be written as:

$$\Delta C = J\Delta\varepsilon \qquad (2)$$

where $\Delta C \in \mathbb{R}^m$ is the change of capacitance due to perturbation, m is the number of independent capacitance measurements. $\Delta\varepsilon \in \mathbb{R}^n$ is the perturbation of permittivity distribution, n is the number of pixels of reconstructed images. $J \in \mathbb{R}^{m \times n}$ is the Jacobian matrix, *i.e.,* the sensitivity of the capacitance to changes in permittivity.

To reconstruct the $\Delta\varepsilon$ from Eq. (2), it can be considered as an optimization problem:

$$\widehat{\Delta\varepsilon} = arg\min_{\Delta\varepsilon}\left\{\frac{1}{2}\|J\Delta\varepsilon - \Delta C\|^2 + \mu L(\Delta\varepsilon)\right\} \qquad (3)$$

where $\widehat{\Delta\varepsilon}$ is the estimated solution of permittivity change; $L(\cdot)$ and $\mu \in \mathbb{R}$ denote the regularization function and parameter, respectively. This optimization problem can be solved by using Tikhonov regularization[14], and the solution of Eq. (3) can be expressed as:

$$\widehat{\Delta\varepsilon} = (J^T J + \mu I)^{-1} J^T \Delta C \qquad (4)$$

However, the conventional ECT ignores the conductivity information of the liquids. For CV-ECT, according to the electromagnetic theory, the complete form of Eq. (1) is rewritten as:

$$C^* = -\frac{1}{V} \iint_S \varepsilon^*(x,y,f)\nabla\phi(x,y)d\Gamma \qquad (5)$$

where C^* denotes the complex-valued capacitance; $\varepsilon^*(x,y,f) = \varepsilon(x,y) + \frac{\sigma(x,y)}{j2\pi f}$ denotes the complex permittivity distribution, where $\sigma(x,y)$ is the conductivity distribution, and f is the frequency of the excitation signal.

In Eq. (5), $\nabla\phi(x,y)$ also depends on $\varepsilon^*(x,y,f)$, so C^* can be considered as a functional of ε^*:

$$C^* = g(\varepsilon^*) \qquad (6)$$

g is the mapping from the change in complex permittivity to the change in complex-valued capacitance. And the linearization of Eq. (6) is:

$$\Delta C^* = J\Delta\varepsilon^* \qquad (7)$$

where the Jacobian matrices J is calculated as:

$$J = \frac{\partial C^*}{\partial \varepsilon^*} \approx \frac{g(\varepsilon_0^* + \Delta\varepsilon^*) - g(\varepsilon_0^*)}{\Delta\varepsilon^*} \qquad (8)$$

where ε_0^* is the complex permittivity of the linearization point, which can be selected as air or water in air-water two phase flows; $\Delta\varepsilon^*$ represents the difference of the complex permittivity distribution between the current phantom and the linearization point.

Since the values in Eq. (7) is complex, the linearization approximation of Eq. (7) can be rewritten as:

$$\begin{bmatrix} \Delta C_r \\ \Delta C_i \end{bmatrix} = \begin{bmatrix} J_{r,\varepsilon} & J_{r,\sigma} \\ J_{i,\varepsilon} & J_{i,\sigma} \end{bmatrix} \begin{bmatrix} \Delta\varepsilon_r \\ \Delta\varepsilon_i \end{bmatrix} \qquad (9)$$

where $\Delta C_r, \Delta C_i$ are the real and imaginary part of the complex capacitance change; $J_{r,\varepsilon}, J_{r,\sigma}$ are the Jacobian matrices mapping the change of permittivity and conductivity to the real part of capacitance change; likewise, $J_{i,\varepsilon}, J_{i,\sigma}$ are the Jacobian matrices mapping the change of permittivity and conductivity to the imaginary part of capacitance change; $\Delta\varepsilon_r$ and $\Delta\varepsilon_i$ denote the real and imaginary part of complex permittivity change, where $\Delta\varepsilon_r$ is the permittivity change and $\Delta\varepsilon_i = -\frac{\Delta\sigma}{2\pi f}$ is the conductivity change.

Similarly, $\Delta\varepsilon_r$ and $\Delta\varepsilon_i$ can be solved by Tikhonov regularization:

$$\begin{bmatrix} \Delta\varepsilon_r \\ \Delta\varepsilon_i \end{bmatrix} = \left(\begin{bmatrix} J_{r,\varepsilon} & J_{r,\sigma} \\ J_{i,\varepsilon} & J_{i,\sigma} \end{bmatrix}^T \begin{bmatrix} J_{r,\varepsilon} & J_{r,\sigma} \\ J_{i,\varepsilon} & J_{i,\sigma} \end{bmatrix} + \begin{bmatrix} \alpha I & 0 \\ 0 & \beta I \end{bmatrix}\right)^{-1} \begin{bmatrix} J_{r,\varepsilon} & J_{r,\sigma} \\ J_{i,\varepsilon} & J_{i,\sigma} \end{bmatrix}^T \begin{bmatrix} \Delta C_r \\ \Delta C_i \end{bmatrix} \qquad (10)$$

where $I \in \mathbb{R}^{m \times n}$ is an identity matrix; α and β are the regularization parameters. The value of α and β are chosen based on a fine-tuning procedure by trials. Thus, $\Delta\varepsilon$ and $\Delta\sigma$ can be calculated at the same time.

III. SIMULATIONS

A. Phantoms in Simulation

An 8-electrode ECT sensor with 60 *mm* external and 56 *mm* internal diameters was used in both simulations and experiments. The sketch of the ECT sensor is shown in Fig. 1. The conventional ECT sensing strategy[14] was adopted, where a complete scan comprises 28 non-redundant complex capacitance measurements.
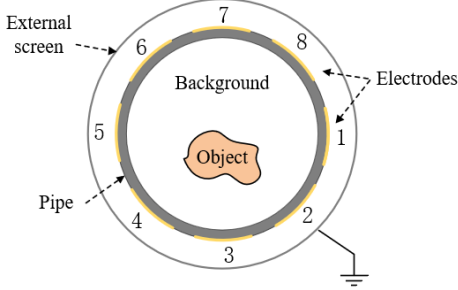

Fig. 1 Structure of the sensor

Sample phantoms include *Phantom A, B* and *C*: an air rod with different diameter (15 *mm*, 25 *mm*, 40 *mm* respectively) in the center of water background; *Phantom D* and *E*: one and two sample rods (diameter is 15 *mm*) positioned near the edge of the sensing area with water background; *Phantom F* and *G*: a water rod with 15 *mm* and 40 *mm* diameter respectively in the center of air background. These phantoms are listed in the first column of TABLE I and TABLE II, where the blue areas represent saline and white areas represent air.

Three excitation frequencies: 0.1 *MHz*, 1 *MHz* and 10 *MHz* are chosen to indicate reconstruction capability of CV-ECT. Two different conductivity values of the saline were tested, *i.e.*, 1e-4 *S/m* and 0.1 *S/m*. Therefore, σ/f is in the range of 1e-5 to 1.0 *S/(m·MHz)*.

B. Noise Setting

To testify the accuracy and stability of reconstructed images, noise is added to the measurements. The experiments were conducted based on an impedance analyzer (Keysight E4990A), so the noisy measurements are set as:

$$C_{noise} = (1 + e_1\%)|C|\angle(\theta + e_2/100) \tag{11}$$

$$|e_i| < E, i = 1,2 \tag{12}$$

where C is the noise-free simulated capacitance measurement, θ is the phase of C and e is the noise randomly generated within the controlled level of E. According to the E4990A Impedance Analyzer data sheet [15], E is set to be 1.

C. Image Quality Assessment

The Structural Similarity Index Measure (*SSIM*) is employed to quantitatively evaluate the reconstruction image quality. *SSIM* is commonly used in the area of image processing to evaluate the similarity between the reconstructed image and the ground truth. The *SSIM* is defined as [16]:

$$SSIM = \frac{(2\mu_x\mu_y + R_1)(2\delta_{xy} + R_2)}{(\mu_x^2 + \mu_y^2 + R_1)(\delta_x^2 + \delta_y^2 + R_2)} \tag{13}$$

where x, y are the reconstructed results and the true distribution, respectively; μ_x, μ_y, δ_x, δ_y, and δ_{xy} denote respectively the local means, standard deviations, and cross-covariance for images x, y; R_1, R_2 are the regularization constants for the luminance and contrast. The value of SSIM is in the range of 0 to 1. The closer *SSIM* is to 1, the better the image quality.

When calculating SSIM, background filter is used to improve the quality of reconstructed images:

$$g`_i = \begin{cases} 0, & |g_i| < |T| \\ g_i, & |g_i| \geq |T| \end{cases} \tag{14}$$

where g_i is the *i*-th pixel of images and $g`_i$ is the *i*-th pixel of images after filtering. T is the threshold selected by Otsu's method [17].

D. Simulation Results

The simulation results reconstructed at both low-conductivity ($\sigma_{water} = 1e - 4\ S/m$) and high-conductivity ($\sigma_{water} = 0.1\ S/m$) water background are listed in TABLE I. In the inverse solver, the linearization point is selected as the sensor is fully filled with water. Therefore, the capacitance difference is calculated by:

$$\Delta C^* = C^*_{phantom} - C^*_{water} \tag{15}$$

where $C^*_{phantom}$ is the measurement of current phantom and C^*_{water} is the measurement of the water-filled sensor. Correspondingly, the Jacobian matrices J is calculated by:

$$J = \frac{g(\varepsilon^*_{water} + \Delta\varepsilon^*) - g(\varepsilon^*_{water})}{\Delta\varepsilon^*} \tag{16}$$

where ε^*_{water} is the complex permittivity of water, and $\Delta\varepsilon^*$ is a small perturbation from ε^*_{water}.

TABLE I SIMULATION RESULTS OF LINEARIZATION AT WATER-FILLED SENSOR

Conductivity, σ (S/m)		0.1		0.1		0.1		1e-4		1e-4		1e-4	
Frequency, f (MHz)		0.1		1.0		10.0		0.1		1.0		10.0	
σ/f (S/(m $\cdot$ MHz))		1.0		0.1		1e-2		1e-3		1e-4		1e-5	
Distribution		$\Delta\varepsilon$	$\Delta\sigma$	$\Delta\varepsilon$	$\Delta\sigma$	$\Delta\varepsilon$	$\Delta\sigma$	$\Delta\varepsilon$	$\Delta\sigma$	$\Delta\varepsilon$	$\Delta\sigma$	$\Delta\varepsilon$	$\Delta\sigma$

Group1   Group2   Group3   Group4

TABLE II SIMULATION RESULTS OF LINEARIZATION AT AIR-FILLED SENSOR

Conductivity, σ (S/m)		0.1		0.1		0.1		1e-4		1e-4		1e-4	
Frequency, f (MHz)		0.1		1.0		10.0		0.1		1.0		10.0	
σ/f (S/(m $\cdot$ MHz))		1.0		0.1		1e-2		1e-3		1e-4		1e-5	
Distribution		$\Delta\varepsilon$	$\Delta\sigma$	$\Delta\varepsilon$	$\Delta\sigma$	$\Delta\varepsilon$	$\Delta\sigma$	$\Delta\varepsilon$	$\Delta\sigma$	$\Delta\varepsilon$	$\Delta\sigma$	$\Delta\varepsilon$	$\Delta\sigma$

Group1   Group2   Group3   Group4

In TABLE I, the images can be divided into four groups according to the reconstruction quality of permittivity and conductivity. Group 1 have red background with crossed lines, in which the reconstruction of permittivity and conductivity distribution both fail; the yellow background with horizontal lines is belong to group 2, where the reconstruction of permittivity fails but the reconstruction of conductivity works; group 3 has green background and both reconstructions are satisfactory; group 4 has blue background with vertical lines, where the reconstruction of permittivity works but the reconstruction of conductivity fails. In the reconstructed images, warm color indicates the higher value of permittivity while cold color indicates the smaller one. Normalized delta permittivity $\Delta\varepsilon = 0$ or normalized delta permittivity $\Delta\sigma = 0$ indicates that the materials remains unaltered and is still the background materials. If water-filled sensor is selected as the linearization point, $\Delta\varepsilon$, $\Delta\sigma = 0$ represents water while $\Delta\varepsilon$, $\Delta\sigma = -1$ represents air. On the contrary, if air-filled sensor is selected as the linearization point, $\Delta\varepsilon$, $\Delta\sigma = 0$ represents air while $\Delta\varepsilon$, $\Delta\sigma = 1$ represents water.

E. Linearization Point Selection

For *Phantom A-E* in TABLE I, the reconstruction of both conductivity and permittivity distribution fail at excitation frequency of $0.1MHz$ for $\sigma_{water} = 0.1\,S/m$, however as the excitation frequency increases to $10MHz$, both distributions could be obtained. On the contrary, for $\sigma_{water} = 1e-4\,S/m$, reducing the excitation frequency from 10 to $0.1MHz$ evidently improves the reconstructed conductivity distribution, where both the size and positions of phantoms can be reconstructed reliably. The reconstructed images suggest that when σ_{water}/f
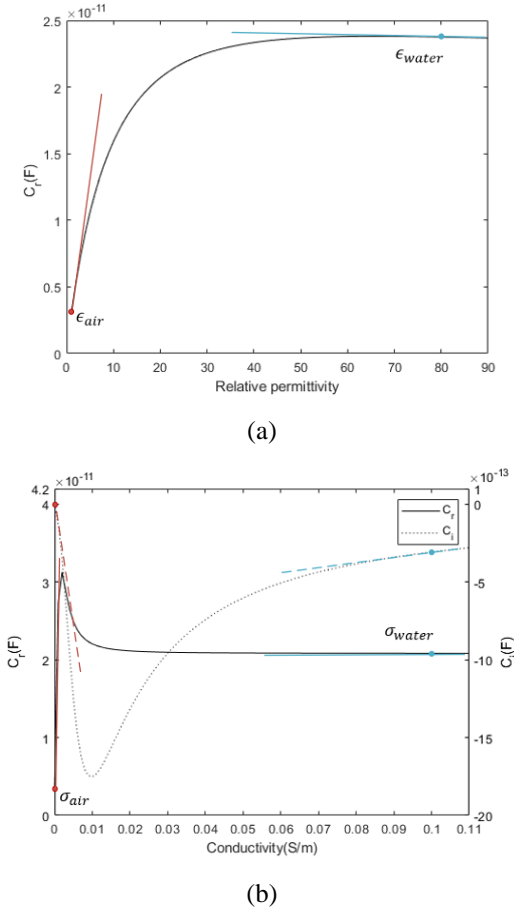
(a)

(b)

Fig. 2 Capacitance measurement between a pair of adjacent electrodes against relative change in permittivity and conductivity (a) relative permittivity from 1 to 90 when conductivity is 0 *S/m*, (b) conductivity from 0 to 0.11 *S/m* when relative permittivity is 1.

fall within the range of 1e-3 and 0.1 *S/(m · MHz)* both permittivity and conductivity distribution can be reconstructed satisfactory. The exceptions are *Phantom F* and *Phantom G*, where the reconstructions fail at all frequencies listed, caused by inappropriate selection of the linearization point, which will be discussed in detail later.

To demonstrate the nonlinearity of the complex capacitance changes with respect to the change in permittivity and conductivity, the relationships between capacitance (one pair of adjacent electrodes) and changing relative permittivity as well as conductivity are plotted in Fig. 2. The slope of the red and the blue tangent line in Fig. 2(a) is the value of sensitivity $J_{r,\epsilon}$ mapping the permittivity change to the capacitance change from the permittivity of air and water, respectively. In Fig. 2(b), the left vertical axis is the real part of complex capacitance and the trend is plotted in full line while the right vertical axis is the imaginary part and the trend is plotted in dashed line. The slope of the red line and the red dashed line is the value of $J_{r,\sigma}$ and $J_{i,\sigma}$ from the conductivity of air while the two blue lines represent $J_{r,\sigma}$ and $J_{i,\sigma}$ from the conductivity of water, respectively. It clearly shows the nonlinear nature of ECT.

To reduce the influence of nonlinearity for *Phantom F* and *G*, air-filled sensor is selected as the linearization point, and the

results are listed in TABLE II. The reconstructions of permittivity and conductivity in *Phantom F* and *G* are accurate when the conductivity is 0.1 *S/m*. For $\sigma_{water} = 1e - 4\ S/m$, the permittivity image is still accurate. Compared with the images in TABLE I, the reconstruction has been greatly improved. It verifies that the quality of reconstruction is based on the selection of the linearization point.

To further indicate the influence of linearization point selection, the trends of the capacitance difference change with σ_{water}/f for *Phantom A* as well as *F* are plotted in Fig. 3 and Fig. 4, respectively. Because of the symmetry of phantoms, four independent capacitance measurements between electrode 1 and electrode 2,3,4,5 are chosen to represent the measurements between different positioned electrodes.

In Fig. 3, C_A is the complex capacitance measurement of *Phantom A*; C_{water} and C_{air} is the complex capacitance measurement when the pipe is full of water and air, respectively. As the Fig. 3(a) shows, at water background, the real part of the complex capacitance change ΔC_r shrink rapidly when the value of σ_{water}/f is higher than 3×10^{-2} *S/(m·MHz)*. The imaginary part of complex capacitance change ΔC_i is rather smaller than ΔC_r when the value of σ_{water}/f is less than 1×10^{-4} *S/(m·MHz)*. With the increase of σ_{water}, ΔC_i become bigger and reaches a peak around $\sigma_{water}/f = 1 \times 10^{-2}$ *S/(m·MHz)* then decline. The trend of the absolute capacitance difference with the change of σ_{water}/f accord with the reconstruction results shown in the TABLE I. The bigger value of the capacitance difference tends to get better reconstruction results because small measurements can be easily influenced by noise and yield distorted results. Moreover, to investigate the influence of the capacitance difference's amplitude, the relative capacitance difference is introduced here: we normalize the capacitance change by using the value of $|C_{water} - C_{air}|$ as the denominator. As Fig. 3(b) shows, the relative capacitance change is much smaller than 1, so the linearity remains valid when water background is selected as the linearization point. The capacitance difference at the linearization point of air is shown in Fig.3(c), which is very different from the capacitance in Fig.3(a). And as Fig.3(d) shows, the amplitude of relative capacitance difference at the linearization point of air is about 1, so the reconstruction results of *Phantom A* in TABLE II are inaccurate due to the nonlinearity.

In Fig. 4, C_F is the complex capacitance measurement of *Phantom F*. C_{water} and C_{air} is the complex capacitance measurement when the pipe is full of water and air respectively. As shown in Fig. 4 (a), the capacitance difference of *Phantom F* at the linearization point of water is similar as the opposite number of the capacitance difference shown in Fig. 3 (c). The amplitude of relative capacitance difference is about 1 in Fig. 4 (b). So, the reconstruction of *Phantom F* at the linearization point of water also failed because of the nonlinearity deviation. As the Fig. 4 (c) shows, at the linearization point of air, the real part of the complex capacitance change ΔC_r almost unchanged when the σ_{water}/f increases and the imaginary part of complex capacitance change ΔC_i is much smaller than ΔC_r. The magnitude of relative capacitance difference in Fig. 4(d) is just 10^{-3}, so the validity of linearization approximation is ensured.
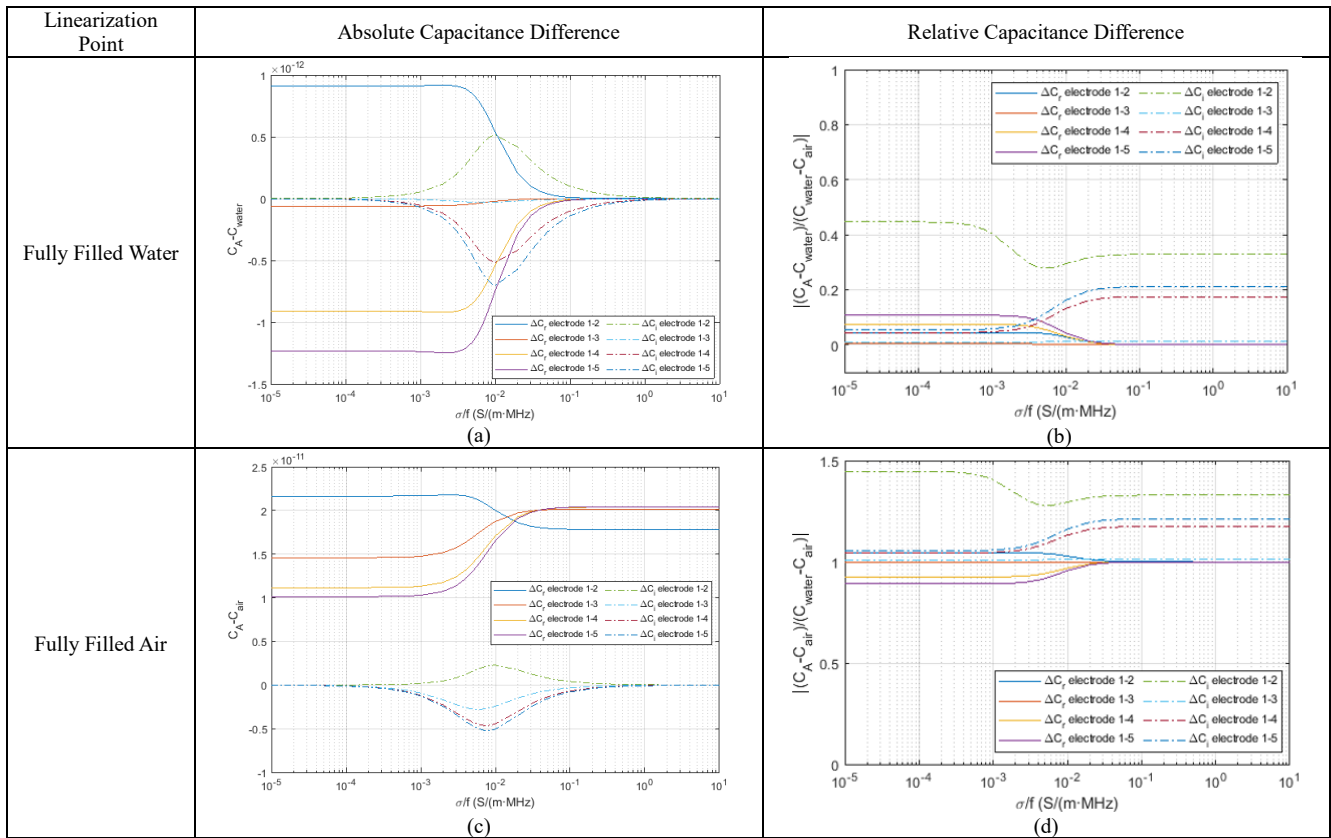
Fig. 3 capacitance difference of *Phantom A* (a) absolute capacitance difference of linearization at fully filled water, (b) relative capacitance difference of linearization at fully filled water, (c) absolute capacitance difference of linearization at fully filled air, (d) relative capacitance difference of linearization at fully filled air
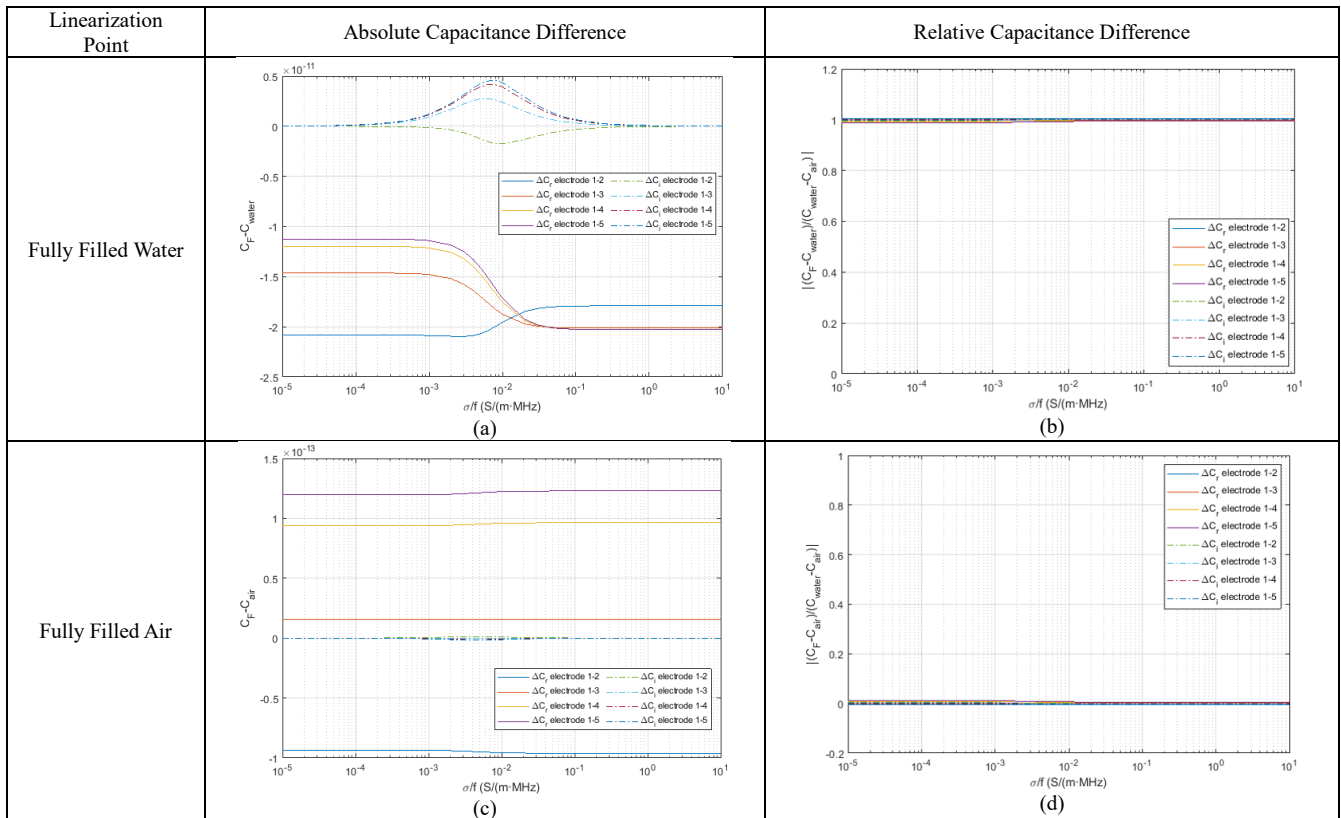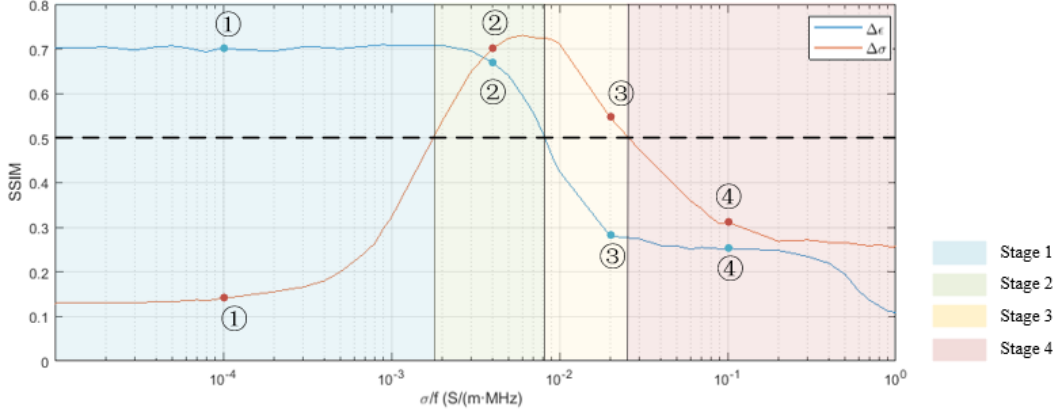

Fig. 4 capacitance difference of *Phantom F* (a) absolute capacitance difference of linearization at fully filled water, (b) relative capacitance difference of linearization at fully filled water, (c) absolute capacitance difference of linearization at fully filled air, (d) relative capacitance difference of linearization at fully filled air
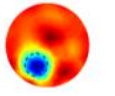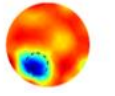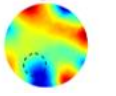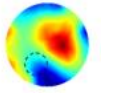
Fig. 5 SSIM of the simulation results of *Phantom D* under water background

TABLE III Typical reconstruction images at the four stages shown in Fig.5
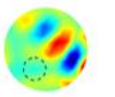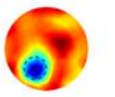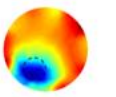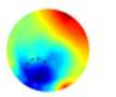
Point	①	②	③	④
σ_{water}/f (S/(m·MHz))	1e-4	4e-3	2e-2	1e-1
$\Delta\varepsilon$				
$\Delta\sigma$				

Selecting the linearization point near the current phantom helps to minimize the impact of the nonlinear inherence of CV-ECT: according to the reconstruction results in TABLE I and TABLE II, the material fills the background within the pipe should be selected as the linearization point to get accurate reconstruction images.

F. Frequency Selection

Besides the linearization point, the capacitance difference in Fig.3 and Fig.4 change with σ_{water}/f. To show the influence of the combination of conductivity and excitation frequency, the image quality *Phantom D* is examined when the σ_{water}/f is swept from 10^{-4} to 1 S/(m·MHz). To quantitatively assess the image quality under different random noise, 1000 sets of measurements at each σ_{water}/f are solved and the average SSIM of these 1000 images are plotted in Fig.5. The trend of SSIM is similar to the magnitude of ΔC_r and ΔC_i shown in Fig. 3(a). The images whose SSIM is higher than 0.5, are acceptable and then the trend can be divided into four stages with different background colors. The meanings of the background colors here are same as the background colors shown in TABLE I. The typical reconstructed distribution of both permittivity and conductivity at σ_{water}/f = 1e-4, 4e-3, 2e-2, 1e-1 S/(m·MHz) are imaged in TABLE III, which can intuitively show how the image quality change with σ_{water}/f. When σ_{water} is low (at stage 1), ΔC_i is very small while ΔC_r is adequate to reconstruct the sample. As σ_{water} increases (at stage 2), both permittivity and conductivity can be well reconstructed. When σ_{water} reaches around 0.01 S/m, the reconstruction of permittivity begins to fail while the reconstruction of conductivity is still satisfactory if σ_{water} continue to increase. At this stage (stage 3), the better results can be obtained by increasing excitation frequency. When σ_{water} is bigger than 0.1 S/m, the reconstruction of permittivity and conductivity both fail even at the highest excitation frequency. In this case, combining other contactless imaging method like MIT is a good solution.

The analysis of Fig. 5 suggests that both $\Delta\varepsilon$ and $\Delta\sigma$ can be better reconstructed at higher excitation frequencies when σ_{water}/f is high, because the influence of decreasing conductivity is the same as increasing excitation frequencies. Therefore the optimal frequency can be approximated by the following relationship:

$$\varepsilon_{water} - \varepsilon_{air} = \frac{\sigma_{water}}{2\pi f_o} \qquad (17)$$

where ε_{water} and σ_{water} is the permittivity and conductivity of water. ε_{air} is the permittivity of air. At the optimal frequency f_o, $\Delta\varepsilon$ and $\Delta\sigma$ have the same impact on capacitance

measurements. For conductivity of water background σ_{water} =0.1 *S/m*, the optimal frequency $f_o = 22.78\ MHz$ and $\frac{\sigma_{water}}{f_o} = 4.39 \times 10^{-3}\ S/(m \cdot MHz))$. The value of $\frac{\sigma_{water}}{f_o}$ is exactly in the center of the horizontal axis at stage 2 in Fig.5, *i.e.*, the reconstruction results of permittivity and conductivity distribution are both satisfactory.

IV. EXPERIMENTAL RESULTS

A. Phantoms and System

Two phantoms are shown in Fig.6: *Phantom 1* in Fig.6(a) has a homogeneous saline background and a circular acrylic bar which diameter is 15 *mm*; *Phantom 2* in Fig.6(b) has the same background but two circular acrylic bars. The experiments of *Phantom 1* and *Phantom 2* at high-conductivity (0.1 *S/m*) and low-conductivity (1e-4 *S/m*) water background were conducted.

The CV-ECT system and an impedance analyzer (Keysight E4990A) are shown in Fig. 7. In the measurement process, we selected a series of excitation frequencies ranging from 0.1 *MHz* to 10 *MHz* with a step of 0.1 *MHz*.

B. Results analysis

TABLE IV presents the experimental results that are reconstructed respectively by CV-ECT and conventional ECT at 0.1 *MHz*, 1 *MHz* and 10 *MHz* excitation frequency. Conventional ECT are usually used to reconstruct the permittivity distribution only, and the measurement is the amplitude of the complex capacitance, *i.e.*, $abs(C_r + C_i)$. The permittivity of water is selected as the linearization point for conventional ECT, and the results are listed in the last line of each phantom in TABLE IV. Similarly, to the simulation results, inappropriate linearization point and excitation frequency result in failed reconstruction.

The SSIM of experimental results are plotted in Fig. 8. As shown in Fig. 8(b) (d), when at low-conductivity (1e-4*S/m*) water background, the SSIM of results reconstructed by conventional ECT are satisfactory because the magnitude of $\frac{\sigma(x,y)}{j2\pi f}$ is so small that $\varepsilon^*(x, y, f) \approx \varepsilon(x,y)$, hence the conventional ECT model is closed to the reality. And the $\Delta\varepsilon$ distribution reconstructed by CV-ECT are better than results reconstructed by conventional ECT because of the additional information of conductivity. As shown in Fig. 8(a) and (c), when water conductivity increases, the conventional ECT gradually become disabled whilst the results of $\Delta\sigma$ reconstructed by CV-ECT are promoted because the conductivity cannot be ignored here. In TABLE IV, at 0.1*S/m* water background and 1*MHz* excitation frequency, $\Delta\sigma$ distribution can roughly show the size and position of samples, but $\Delta\varepsilon$ distribution can hardly distinguish the samples. In addition, the SSIM of reconstructed images from the experimental data tends to be improved when the excitation frequency increase at 0.1*S/m* water background.
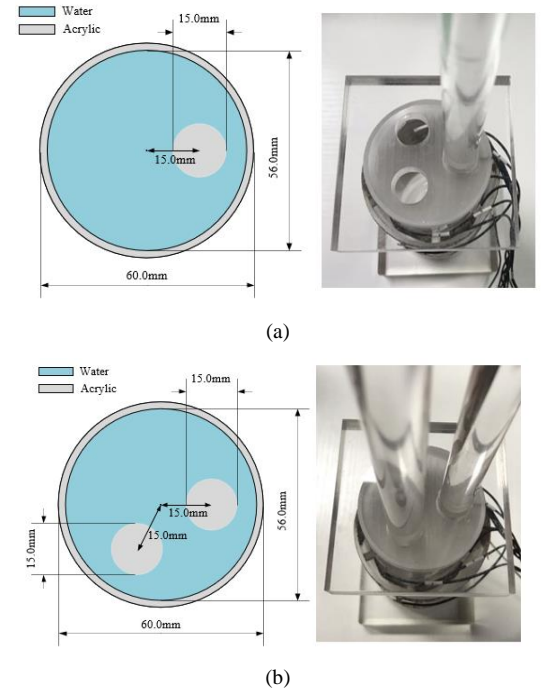

(a)

(b)

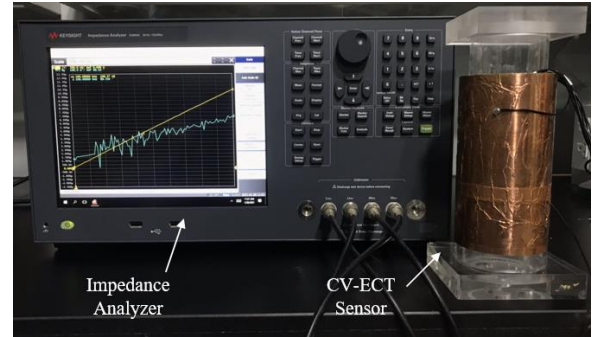Fig. 6. Experimental phantoms. (a) *Phantom 1*. (b) *Phantom 2*.

Fig. 7 The CV-ECT system

V. CONCLUSIONS

This paper introduces CV-ECT system and testify its feasibility through both simulations and experiments. As an improved method of conventional ECT, CV-ECT can measure the conductive multi-phase flows and reconstruct both permittivity and conductivity distribution simultaneously based on the same sensor head of conventional ECT. To ensure the validity of linearization approximation, the linearization point near the current phantom should be selected, *i.e.*, the material around the pipe wall should be chosen as the linearization point to get better reconstruction results. Otherwise, more complicated iterative algorithms will be introduced to solve this highly nonlinear problem. After the selection of the linearization point, the capacitance difference and the appropriate sensitivity matrix can be calculated. Because of the conductivity, the value of the capacitance difference is coupled with the excitation frequency.

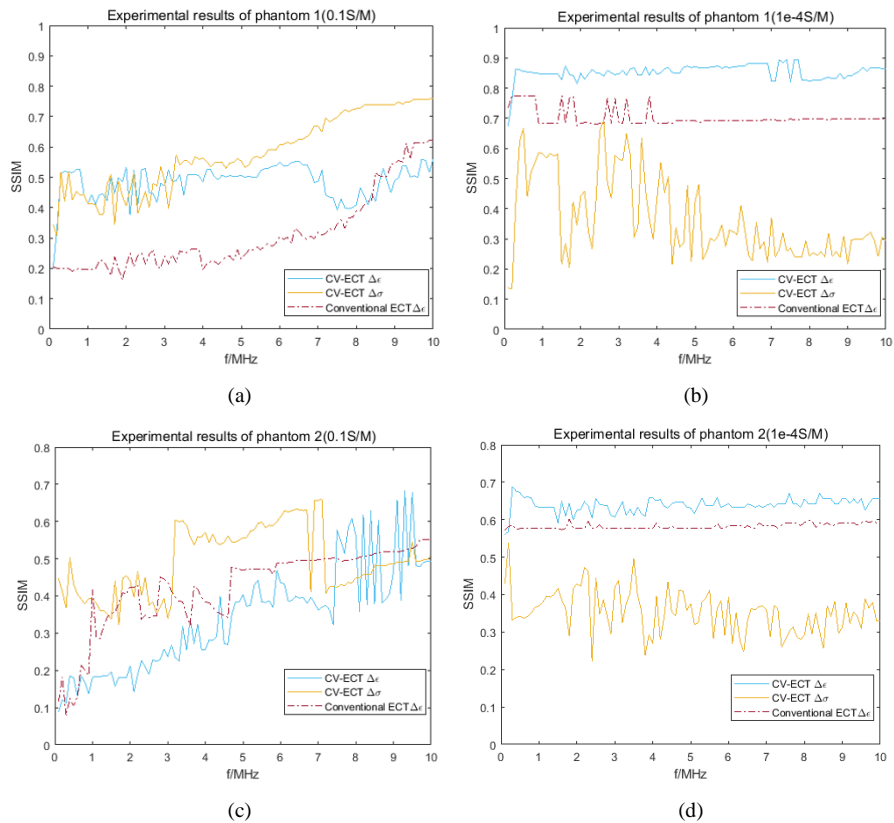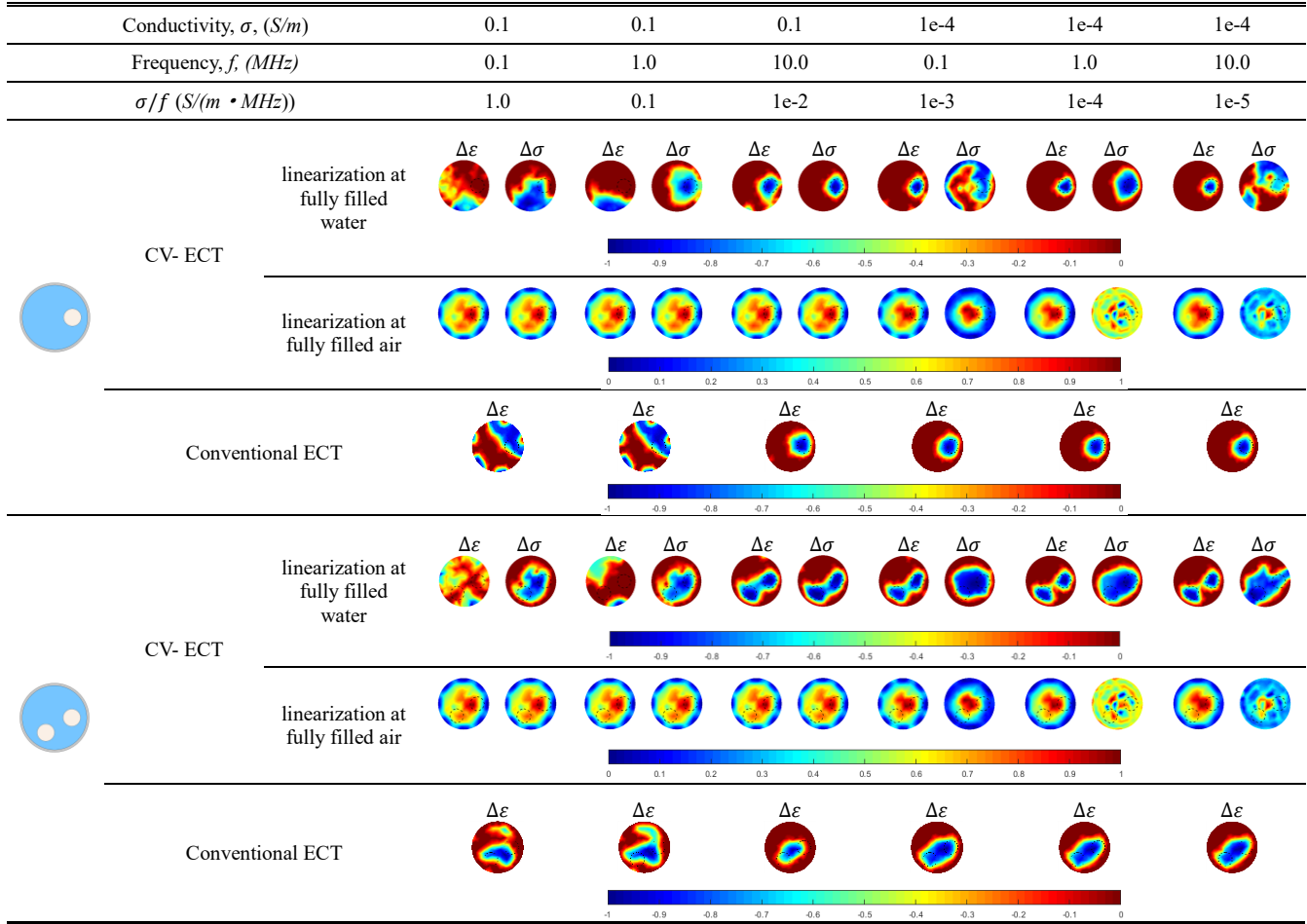TABLE IV EXPERIMENT RESULTS OF CVECT AND CONVENTIONAL ECT

Conductivity, σ, (S/m)	0.1	0.1	0.1	1e-4	1e-4	1e-4
Frequency, f, (MHz)	0.1	1.0	10.0	0.1	1.0	10.0
σ/f (S/(m · MHz))	1.0	0.1	1e-2	1e-3	1e-4	1e-5

Fig.8 SSIM of the experimental results reconstructed by CV-ECT and conventional ECT (a) of *Phantom 1* at 0.1*S/m* water background, (b) of *Phantom 1* at 1e-4*S/m* water background, (c) of *Phantom 2* at 0.1*S/m* water background, (d) of *Phantom 2* at 1e-4*S/m* water background.

quality of reconstruction images in the measurement of high conductivity water, *i.e.,* the value of σ_{water}/f can be adjust to stage 2 (in Fig.5), since the conductivity of the material under test cannot be changed in most real applications. If the conductivity is very high in the industrial applications, and the CV-ECT might not be able to work due to the limited capability of the measurement unit to increase the excitation frequency, therefore other contactless imaging method like MIT can be considered to assist the reconstruction and more effective reconstruction algorithms can be adopted.

REFERENCES

[1] Y. Li *et al.*, "Gas/oil/water flow measurement by electrical capacitance tomography," *Measurement ence & Technology,* vol. 24, no. 7, p. 074001, 2011.

[2] M. Zhang, L. Zhu, H. Wang, Y. Li, M. Soleimani, and Y. Yang, "Multiple Measurement Vector Based Complex-Valued Multi-Frequency ECT," *IEEE Transactions on Instrumentation and Measurement,* 2020, doi: 10.1109/TIM.2020.3045842.

[3] J. Sun and W. Yang, "A dual-modality electrical tomography sensor for measurement of gas–oil–water stratified flows," *Measurement,* vol. 66, pp. 150-160, 2015.

[4] M. Zhang, L. Ma, and M. Soleimani, "Dual modality ECT-MIT multi-phase flow imaging," *Flow Measurement and Instrumentation,* vol. 46, pp. 240-254, 2015.

[5] D. Hu, Z. Cao, S. Sun, J. Sun, and L. Xu, "Dual-Modality Electrical Tomography for Flame Monitoring," *Sensors Journal IEEE,* vol. 18, no. 21, pp. 8847-8854, 2018.

[6] J. K. Seo, J. Lee, S. W. Kim, H. Zribi, and E. J. Woo, "Frequency-difference electrical impedance tomography (fdEIT): algorithm development and feasibility study," *Physiological Measurement,* vol. 29, no. 8, pp. 929-944, 2008.

[7] B. Wang, Z. Gui, W. Tan, Z. Huang, and H. Li, "A new dual-modality ECT/ERT technique based on C4D principle," *Conference Record - IEEE Instrumentation and Measurement Technology Conference,* vol. 2015, no. 5, pp. 2061-2065, 2015.

[8] W. Tan, B. Wan, Z. Huang, H. Ji, and H. Li, "New Image Reconstruction Algorithm for Capacitively Coupled Electrical Resistance Tomography," *IEEE Sensors Journal,* 2017.

[9] G. Ma and M. Soleimani, "Spectral capacitively coupled electrical resistivity tomography for breast cancer detection," *IEEE Access,* vol. PP, no. 99, pp. 1-1, 2020.

[10] C. Gunes, Q. M. Marashdeh, and F. L. Teixeira, "A Comparison Between Electrical Capacitance Tomography and Displacement-Current Phase Tomography," *IEEE Sensors Journal,* vol. PP, no. 24, pp. 1-1, 2017.

[11] Y. Jiang and M. Soleimani, "Capacitively Coupled Phase-based Dielectric Spectroscopy Tomography," *Scientific Reports,* vol. 8, no. 1, 2018.

[12] M. Zhang and M. Soleimani, "Simultaneous reconstruction of permittivity and conductivity using multi-frequency admittance measurement in electrical capacitance tomography," *Measurement ence and Technology,* vol. 27, no. 2, pp. 025405-, 2016.

[13] A. Adler and A. Boyle, "Electrical Impedance Tomography: Tissue Properties to Image Measures," *IEEE Transactions on Biomedical Engineering,* vol. PP, no. 99, pp. 1-1, 2017.

[14] W. Q. Yang and L. Peng, "Image reconstruction algorithms for electrical capacitance tomography," *Measurement science and technology,* vol. 14, no. 1, pp. R1 %@ 0957-0233, 2002.

[15] E4990A Impedance Analyzer Data Sheet [Online] Available: http://literature.cdn.keysight.com/litweb/pdf/5991-3890EN.pdf

[16] Z. Wang, "Image Quality Assessment : From Error Visibility to Structural Similarity," *IEEE Transactions on Image Processing,* 2004.

[17] N. Otsu, "A Threshold Selection Method from Gray-Level Histograms," *IEEE Transactions on Systems Man & Cybernetics,* vol. 9, no. 1, pp. 62-66, 2007.